Original Article
ISSN (Online): 2582-7472

ShodhKosh: Journal of Visual and Performing Arts
February 2024 5(2), 1213–1223

INVESTIGATION ON THE STRUCTURAL, MAGNETIC, AND DIELECTRIC PROPERTIES OF MG2+ SUBSTITUTED NI-CD-IN SPINEL NANOSTRUCTURED FERRITES SYNTHESIZED BY COPRECIPITATION ROUTE

Gaurav Kale [1], Dilip S. Badwaik [2] ✉, Dnyaneshwar D. Mathankar [3], Sarang R. Daf [4], Shrikant M. Suryawanshi [2]

[1] Shri Vitthal Rukhmini Mahavidyalaya, Sawana (M.S)- 445205, India
[2] Kamla Nehru Mahavidyalaya, Nagpur (M.S)-440024, India
[3] V.P. Arts and Science College, Borgadi, Pusad -445215, India
[4] Shri Shivaji Science College, Nagpur (M.S)-440012, India

Corresponding Author
Dr. Dilip S Badwaik,
badwaik_ds@rediffmail.com

DOI
10.29121/shodhkosh.v5.i2.2024.5055

Funding: This research received no specific grant from any funding agency in the public, commercial, or not-for-profit sectors.

ABSTRACT

A soft spinel ferrite has the chemical formula MgxNi0.6Cd0.4-xFe2-yInyO4, where X values are 0.0, 0.1, 0.2, 0.3, and 0.4, and y is fixed at 0.05. These are labelled as GK6, GK7, GK8, GK9, and GK10 and are made using the coprecipitation method. X-ray diffraction patterns show that the crystallite size decreases from 21 nm to 10 nm, and the lattice dimension shrinks from 8.4839 to 8.4175 Å. FTIR analysis shows a strong vibrational band for the Fe-O group between 400 and 4000 cm^{-1}, which confirms the formation of spinel ferrite. VSM analysis indicates that coercivity increases from 297 to 338 Oe. However, retentivity decreases from 8.87 to 1.99 emu/g, and magnetic saturation drops from 54 to 22 emu/g. The impedance analyzer shows lower losses at high frequencies, suggesting that this material is suitable for microwave devices.

Keywords: XRD, FTIR, VSM and Dielectric Spectroscopy

1. INTRODUCTION

Spinel nanoferrites represent a unique class of magnetic materials characterized by their distinct AB2O4 crystal structure [1]. In this structure, metal cations, designated as A and B, occupy tetrahedral and octahedral sites, respectively, within a three-dimensional cubic lattice formed by oxygen ions [2]. At the nanoscale, these materials exhibit a range of fascinating properties that distinguish them from their bulk counterparts, including superparamagnetism, which allows them to respond rapidly to changing magnetic fields without retaining magnetization; a high surface area that enhances reactivity; and quantum confinement effects that can lead to altered electronic and optical behaviour [3].

The remarkable properties of spinel nanoferrites can be fine-tuned by manipulating various factors, including the chemical composition of the metal cations, the size of the nanoparticles, and the methods employed for their synthesis [4,5]. For instance, varying the ratio of A and B cations can significantly affect the magnetic saturation and coercivity, while controlling the particle size during synthesis can enhance their superparamagnetic behaviour and improve their performance in applications. Due to these versatile properties, spinel nanoferrites hold promising potential in a wide array of applications. They are being actively explored for high-density data storage solutions, where their superparamagnetic characteristics enable the storage of vast amounts of information in compact formats[6-8]. Additionally, their high surface area and biocompatibility make them suitable candidates for targeted drug delivery systems, allowing for the precise transport of therapeutic agents to specific tissues or cells. Furthermore, their catalytic properties are being investigated for various chemical processes, offering possibilities for improved efficiency and selectivity in industrial applications [9,10].

Overall, the tunability and multifunctionality of spinel nanoferrites position them as key materials in advancing technologies across fields such as information technology, medicine, and catalysis.

Recent research has successfully synthesized Magnesium (Mg) doped Nickel-Cadmium-Indium) (NiCdIn) spinel ferrite nanoparticles using a cost-effective and scalable co-precipitation method. This technique allows for precise control over the material's initial composition. A thorough investigation was conducted to assess the physical and chemical properties of the synthesized nanoparticles, focusing on their structural, morphological, magnetic, and electrical characteristics. The study aims to evaluate the viability of these nanoferrites for various applications in advanced electronic devices, highlighting their potential in the rapidly evolving field of electronic technology.

2. SYNTHESIS AND CHARACTERIZATION

The study focused on the preparation of the compound MgxNi0.6Cd0.4-xFe2-yInyO4, where the variable x took values of 0.0, 0.1, 0.2, 0.3, and 0.4, while y remained fixed at 0.05. The synthesis was carried out using the co-precipitation method. Initially, a solution containing divalent metal ions, comprising 0.2 M solutions of Magnesium Chloride, Nickel Chloride, and Cadmium Chloride, was prepared alongside a separate 0.4 M solution of trivalent metal ions, which included Iron Chloride and Indium Chloride, both dissolved in 40 ml of double-distilled water. After ensuring homogeneity through 15 minutes of stirring, the two solutions were combined and heated to 80°C with continuous stirring. To adjust the pH to 12, 4 M sodium hydroxide was introduced. The resulting solution underwent multiple rounds of filtration (3-5 times) using double-distilled water and ethanol, followed by drying for 2 hours at 100°C in an oven. The dried material was then ground for 3 hours using a mortar and pestle before being calcined at 800°C for 5 hours and ground again for an additional hour to achieve a fine powder form. The final samples were designated as GK6, GK7, GK8, GK9, and GK10.

The microstructural properties of these samples were analyzed with an X-ray diffractometer (Bruker D8 Advance) using a wavelength of 1.5406 Å. Functional groups were examined using Fourier Transform Infrared Spectroscopy (FTIR) in the range of 400 cm^{-1} to 4000 cm^{-1} with a Shimadzu IR Affinity–1. Magnetic properties were assessed through magnetization versus field (M-H) loop measurements using a Vibrating Sample Magnetometer (VSM), while dielectric properties were recorded with impedance spectroscopy (Model: PSM 1735).

3. RESULTS AND DISCUSSION

3.1. X-RAY DIFFRACTION

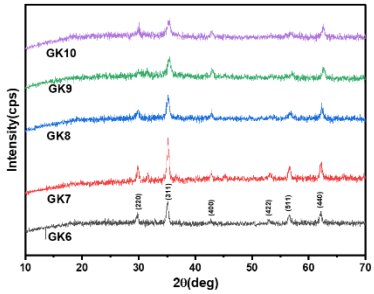

Figure 1 X-ray diffraction of as synthesized GK6, GK7, GK8, GK9, and GK10 Spinel Ferrite

The X-ray diffraction patterns for the synthesized compounds MgxNi0.6Cd0.4-xFe2-yInyO4, where the variable x took values of 0.0, 0.1, 0.2, 0.3, and 0.4, while y remained fixed at 0.05 are denoted as GK6, GK7, GK8, GK9, and GK10, respectively(Figure 1). The diffracted peaks observed correspond to the indices (111), (220), (311), (222), (400), (422), (511), and (440), indicating that the materials exhibit a cubic/spinel structure typical of ferrite compounds. This crystalline arrangement belongs to the space group Fd-3m, highlighting the synthesized ferrites' structural integrity and phase purity[11] In Table 1, various microstructural parameters derived from the diffraction pattern are presented. Notably, the peak position (2θ) for series, GK6 to GK6, shows a progressive increase from 35.05 degrees to 35.34 degrees. Correspondingly, the Full Width at Half Maximum (FWHM, β) also exhibits an increase from 0.45 degrees to 0.77 degrees. This rise in peak position indicates a decrease in interplanar spacing (d), suggesting a contraction in the overall size of the unit cell [12]. The crystallite size (D) and lattice dimension(a) for the prepared samples were calculated for most intense peak(311) using Eq.(1) and (2) and estimated in Table1

$$D = \frac{0.9\lambda}{\beta \cos\theta} \qquad (1)$$

$$a = d_{hkl}\sqrt{h^2 + k^2 + l^2} \qquad (2)$$

Where,λ=1.54060 A°,β=FWHM(Full Width Half Maxima),θ=Peak Position, d-Interplanar Spacing, and (h k l) are the Miller Indices.

Table 1: Peak position (2θ), FWHM (β), interplanar spacing(d-spacing), lattice dimension(a.),crystallite size(D), Lattice Strain(ε), Dislocation density(δ), of GK1 to GK5 Spinel ferrite

Sample	**2θ (deg.)**	**β (deg)**	**d-spacing (Å)**	**a (Å)**	**D (nm)**	**Ɛ x 10^{-3}**	**δ x 10^{-3}** lines/nm^2
GK6	35.05	0.45	2.558	8.4839	18.52	6.214	2.91
GK7	35.16	0.38	2.5502	8.458	21.94	5.23	2.07
GK8	35.14	0.55	2.552	8.464	15.15	7.575	4.35
GK9	35.44	0.54	2.5306	8.393	15.45	7.37	4.18
GK10	35.34	0.77	2.538	8.4175	10.83	1.054	8.52

In Table 1, the observations reveal a notable decrease in both crystallite size and lattice dimensions within the synthesized materials. This intriguing phenomenon can be largely attributed to the introduction of magnesium ions during the synthesis process, which appears to play a pivotal role in modifying the growth kinetics of the resultant structures. The presence of magnesium ions, characterized by a smaller ionic radius of 0.72 Å, stands in contrast to the larger cadmium ions (0.97 Å) [13,14]. This size disparity facilitates a contraction in the unit cell dimensions, promoting the formation of smaller crystalline domains. Furthermore, the addition of indium ions, also measuring 0.91 Å[15], reinforces this contraction effect, leading to a more compact lattice structure. The substitution of magnesium ions not only impacts the lattice parameters but also significantly enhances the stability and overall properties of the ferrite material. This characteristic positioning of magnesium ions emerges as a key factor influencing the comprehensive behaviour of the synthesized materials, highlighting its importance in tailoring material properties for specific applications.

The lattice strain(ε) and the dislocation per unit volume (δ) of the prepared material was calculated using Eq(3) and Eq(4) and estimated in Table 1

$$\varepsilon = \frac{\beta}{4\tan\theta} \qquad (3)$$

$$\delta = \frac{1}{D^2} \qquad (4)$$

The observed lattice strain for the prepared samples, specifically GK6 to GK9, exhibited a notable increase, rising from 6.214 x 10^{-3} to 7.757 x 10^{-3}. This increase is particularly interesting when considering GK10, which displayed a significantly lower lattice strain measurement of only 1.0541 x 10^{-3}. The increase in strain across the samples can be attributed primarily to the substitution of larger cadmium ions (Cd^{2+}) with smaller magnesium ions (Mg^{2+}) within the spinel lattice structure. This ionic substitution introduces a variation in ionic radii, leading to pronounced local lattice distortions. The smaller Mg^{2+} ions create spatial discrepancies in the lattice, resulting in increased local stresses. Furthermore, the incorporation of indium ions (In^{3+}) alongside Mg^{2+} and Cd^{2+} in samples GK6 to GK9 adds another layer of complexity to these lattice dynamics. The differences in ionic size between these substituents generate additional distortions and stresses, compounding the overall increase in lattice strain[16].

The observed variation in dislocation density among the samples .This can be attributed to the incorporation of In^{3+} ions and the subsequent replacement of Mg^{2+} ions for Cd^{2+} ions. This substitution process induces a notably more disordered arrangement of cations within the tetrahedral (A) and octahedral (B) sites of the crystal lattice. As a result, the internal stresses within the material are heightened, leading to an increased likelihood of dislocation formation. These dislocations act as a mechanism for the material to alleviate the internal strains, ultimately contributing to the enhanced dislocation density[17,18].

Additionally, other microstructural parameters such as the ionic radii at tetrahedral sites (rA) and octahedral sites (rB), the cation-anion distance at A-sites (tetrahedral bond length dAX), the cation-anion distance at B-sites (octahedral bond length dBX), and the hopping lengths (dA) and dB) at both A and B-sites were calculated from the lattice parameter of the prepared material[19]. These calculations are presented in Table 2, using equations (5) through (10).

$$r_A = (u - \frac{1}{4})\, a\sqrt{3} - R_0 \qquad (5)$$

$$r_B = (\frac{5}{8} - u)\, a - R_0 \qquad (6)$$

$$d_{AX} = (u - \frac{1}{4})a\sqrt{3} \qquad (7)$$

$$d_{BX} = a\,(3u^2 - \frac{11}{4}u + \frac{43}{64})^{1/2} \qquad (8)$$

$$d_A = a\,\frac{\sqrt{3}}{4} \qquad (9)$$

$$d_B = a\,\frac{\sqrt{2}}{4} \qquad (10)$$

where, is oxygen positional parameter (=0.384 Å) and radius of oxygen (=1.32 Å) for spinel ferrite.

Table 2: Ionic radii at tetrahedral sites (rA) and octahedral sites (rB), along with the cation-anion distances at A-sites (tetrahedral bond length dAX) and B-sites (octahedral bond length dBX), and the hopping lengths (dA) at A-sites and (dB) at B-sites for GK6 to GK10 spinel ferrite.

Samples	$\mathbf{r_A}$	$\mathbf{r_B}$	$\mathbf{d_{AX}}$	$\mathbf{d_{BX}}$	$\mathbf{d_A}$	$\mathbf{d_B}$
	(Å)	(Å)	(Å)	(Å)	(Å)	(Å)
GK6	0.6482	0.7246	1.9682	2.0446	3.6736	2.9995

GK7	0.6422	0.7183	1.9622	2.0383	3.6624	2.9903
GK8	0.6436	0.7198	1.9636	2.0398	3.665	2.9924
GK9	0.6271	0.7027	1.9471	2.0227	3.6342	2.9673
GK10	0.6328	0.7086	1.9528	2.0286	3.6448	2.976

The ionic radius decreases from GK6 to GK10 series, dropping from 0.6482 Å to 0.6271 Å at the tetrahedral site. A similar trend is observed at the octahedral sites (rB), where values range from 0.7246 Å to 0.7027 Å for GK6 to GK10. This pattern is also reflected in the cation-anion distances at A-sites, known as tetrahedral bond lengths (dAX), which decrease from 1.9682 Å to 1.9528 Å. Likewise, the cation-anion distances at B-sites, or octahedral bond lengths (dBX), show a reduction from 2.0446 Å to 2.0227 Å. The hopping lengths (dA) and (dB) consistently decline across the series as well. At the A sites, hopping lengths for GK6 to GK10 decrease from 3.6736 Å to 3.6342 Å, while at the B sites, they drop from 2.9995 Å to 2.9673 Å. These observed decreasing trends in all parameters can be linked to changes in lattice dimensions, primarily driven by the presence of Mg, Cd, and In ions.

3.2. FUNCTIONAL GROUP ANALYSIS

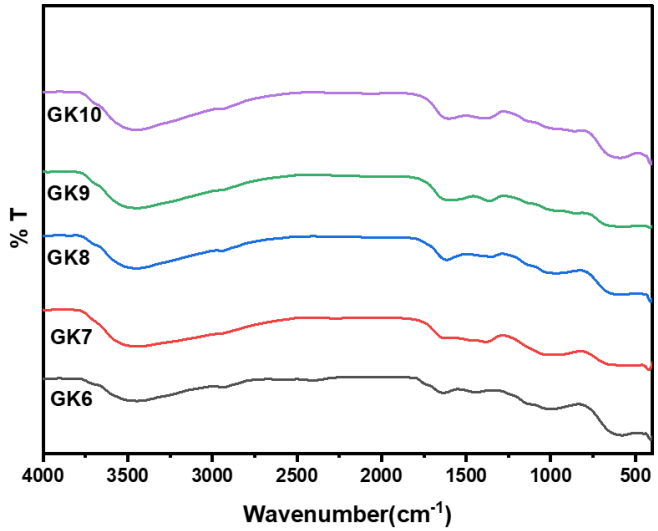

Figure 2 FTIR Spectra of synthesized GK6, GK7, GK8, GK9, and GK10 Spinel Ferrite

Table 3: Vibration band at tetrahedral(νA) and Octahedral site(νB)), Force constant at tetrahedral(kA) and Octahedral site(kB) of GK6 to GK10 Spinel ferrite

Samples	**ν_A**	**ν_B**	**k_A (10^2 N/m)**	**k_B (10^2 N/m)**
	(cm^{-1})	**(cm^{-1})**		
GK6	580	443	2.46	1.43
GK7	571	428	2.38	1.34
GK8	582	420	2.48	1.29
GK9	586	412	2.36	1.24
GK10	588	408	2.53	1.21

In the FTIR spectra, we consistently identify two distinct stretching vibrations linked to the metal-oxygen (Me-O) bonds characteristic of spinel ferrites[20]. A prominent absorption peak observed between 571 and 588 cm^{-1} is associated with vibrations at tetrahedral sites (νA), while another significant peak, located between 408 and 443 cm^{-1}, corresponds to octahedral sites (νB)(Table 3). The data indicate that the vibrational frequency at tetrahedral sites (νA)

is considerably higher than that at octahedral sites (νB). Additionally, we observe that the shifts in vibrational frequencies at both tetrahedral (νA) and octahedral (νB) sites are directly related to the substitution of Mg^{2+} and In^{3+} ions, respectively. The force constant of respective sites can be calculated using Eq(11) and (12)

$$k_A = 4\pi^2 c^2 \nu_A{}^2 \, m_A \qquad (11)$$

$$k_B = 4\pi^2 c^2 \nu_B^2 \, m_B \qquad (12)$$

The measured force constants at both tetrahedral and octahedral sites show an increase, which can be explained by the positional band shifts resulting from the migration of Fe ions from octahedral to tetrahedral sites[21,22].

3.3. SCANNING ELECTRON MICROSCOPE (SEM)

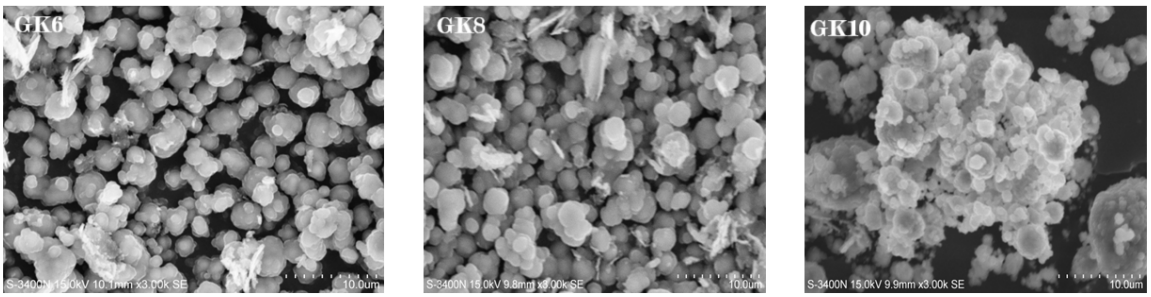

Figure 3 SEM Micrograph of GK6, GK8, and GK10 spinel Ferrite

Figure 3 displays scanning electron microscope (SEM) images of the ferrite samples GK6, GK8, and GK10. The introduction of Mg2+ and In3+ ions in these samples significantly alters the microstructure of the resulting spinel ferrite. Distinct microstructural changes were noted, particularly in the form of particle aggregation. Additionally, the presence of In3+ ions in GK6 and GK8 resulted in noticeable segregation within the microstructure. Furthermore, GK10 showed an increased level of aggregation, likely due to its higher Mg ion concentration. These findings highlight the complex relationship between minor changes in chemical composition and their substantial impact on the microstructural properties of spinel ferrites.

3.4. TRANSMISSION ELECTRON MICROSCOPE (TEM)

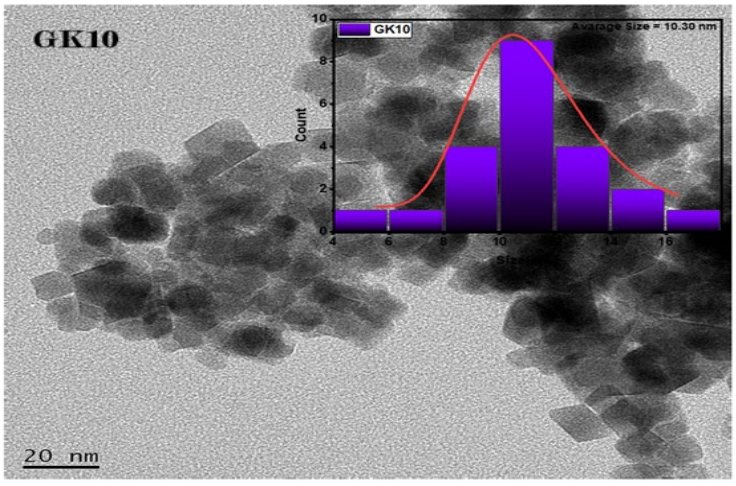

Figure 4 TEM micrograph of prepared GK10 Spinel Ferrite

Figure 4 displays the TEM micrographs of the synthesized GK10 spinel ferrites, which exhibit a nearly cubic morphology and a predominantly spherical shape, with an average particle size of 10.30 nm as determined from the histogram. The micrograph also indicates the presence of agglomerations, which are attributed to magnetic interactions among the nanoparticles that possess a high surface area and energy[23,24]. The agglomeration of these nanoparticles primarily results from interfacial surface tension and magnetostatic interactions, stemming from exchange interactions and the high reactivity of the ferrite samples[25]. These agglomerations manifest as clusters of nanoparticles, as seen in the micrograph. Additionally, the analysis indicates that the particle sizes obtained from TEM are smaller than the crystallite sizes (D) measured by XRD. This difference arises because XRD assesses the size of coherently diffracting crystalline domains, whereas TEM measures the physical size of individual particles. Consequently, if a particle comprises multiple crystallites, the size measured by TEM will be less than the crystallite size determined from XRD.

3.5. M-H LOOP ANALYSIS

The magnetic properties of the prepared material were investigated by M-H loop. The observed saturation magnetization (Ms), coercivity (Hc), and retentivity (Mr) for these as-prepared samples are derived from the figure and compiled in Table 4

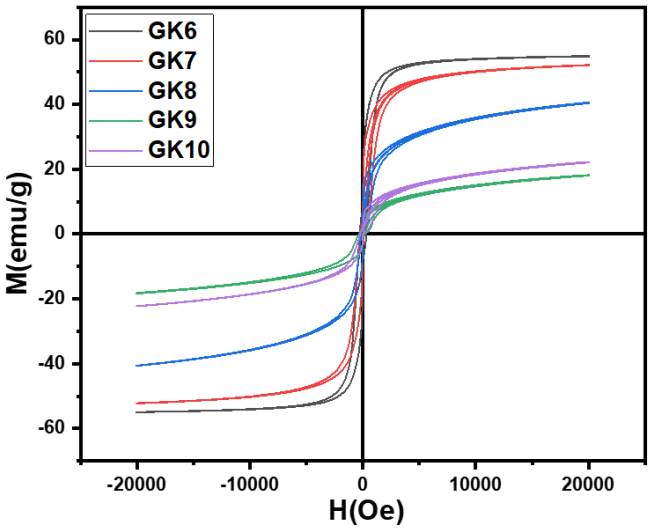

Figure 3 M-H loop of of synthesized GK6, GK7, GK8, GK9, and GK10 Spinel Ferrite

The magnetic characteristics of the MgxNi0.6Cd0.4-xFe2-yInyO4 spinel ferrite system, which varies in magnesium content (x) while maintaining a constant indium level (y = 0.05), demonstrate a complex relationship with composition. The saturation magnetization (Ms) initially declines as x increases from 0.0 to 0.3, likely due to the substitution of magnetic Ni^{2+} ions with non-magnetic Mg^{2+}, resulting in a dilution of the overall magnetic moment. However, at x = 0.4, Ms unexpectedly rises, indicating a potential shift in cation distribution that allows more Fe^{3+} ions to occupy the octahedral sites, thereby enhancing the net magnetization[26,27]. The coercivity (Hc) exhibits a non-linear pattern, first decreasing and then increasing, which suggests a complex interaction of factors such as magnetocrystalline anisotropy and microstructural changes driven by the varying Mg content. Likewise, the remanence (Mr) and the Mr/Ms ratio initially decrease before experiencing a slight increase, reflecting the trends observed in Ms and anisotropy, and indicating alterations in domain structure and interparticle interactions. The magnetocrystalline anisotropy (K) generally diminishes with increasing x up to 0.3, as anticipated due to the reduced concentration of anisotropic Ni^{2+} ions, but it increases at x = 0.4, possibly associated with the modified cation distribution. The small, constant amount of indium likely affects these properties by altering cation site preferences and introducing lattice strain. In summary, the magnetic behaviour observed is a consequence of the intricate interplay between cation substitution, their distribution within the spinel lattice, the resulting changes in magnetic interactions and anisotropy, and potentially subtle variations in the material's microstructure.

Table 4: Coercivity(Hc), Retentivity(Mr), Magnetic Saturation(Ms), Mr/Ms and Anisotropy of GK6 to GK10 Spinel ferrite

Samples	H_c (Oe)	M_r (emu/g)	M_s (emu/g)	M_r/M_S	$Kx10^3$ (erg/g)
GK6	297	8.87	54.88	1.61	16.63
GK7	219	4.67	52.14	0.08	11.65
GK8	212	3.76	40.55	0.09	8.77
GK9	226	1.09	18.20	0.05	4.19
GK10	338	1.99	22.23	0.08	7.66

3.3. DIELECTRIC SPECTROSCOPY

Figure 4 and 5 demonstrates the dielectric characteristics of the prepared samples, highlighting their reactions to electric fields. The dielectric constant and loss, essential for comprehending the material's electrical behaviour, were determined using Eq. (13) and Eq.(14). This analysis offers important insights into the samples' performance and their potential uses in a range of electronic devices.

$$\varepsilon' = \frac{Ct}{\varepsilon_0 A} \qquad (13)$$

$$tan\,\delta = \frac{\varepsilon''}{\varepsilon'} \qquad (14)$$

This equation takes into account the sample's capacitance, thickness, the dielectric permittivity of air (ε_0), and its surface area (A). The real part (ε') indicates the sample's dielectric constant, while the imaginary part (ε") represents the dielectric loss.

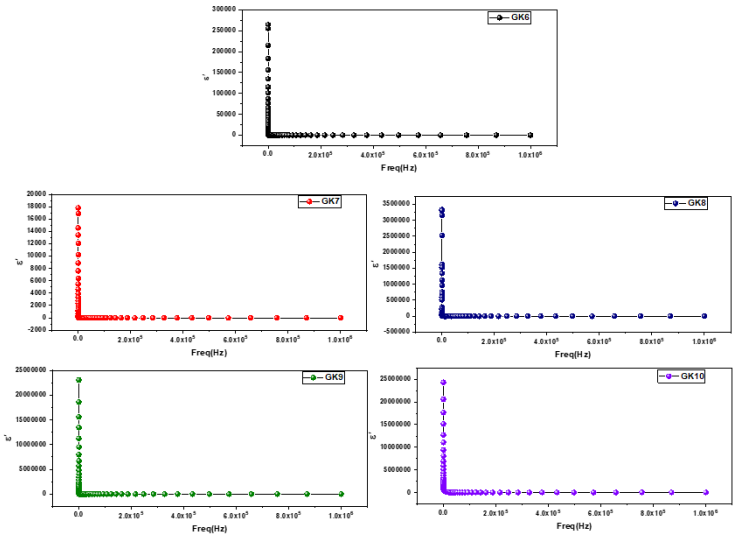

Figure 4 Dielectric Constant of GK6 to GK10 Spinel Ferrite

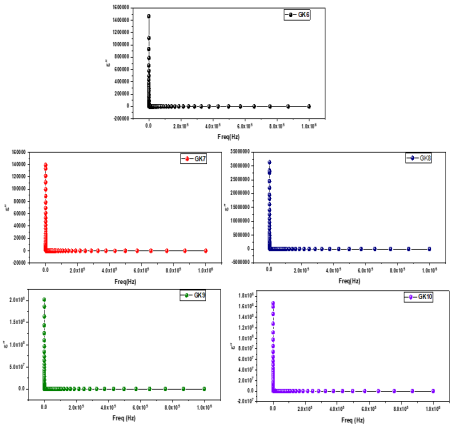

Figure 5 Dielectric Loss of GK6 to GK10 Spinel Ferrite

The dielectric properties of the MgxNi0.6Cd0.4-xFe2-yInyO4 spinel ferrite series (GK6-GK10) exhibit a strong dependence on both the magnesium content (x) and the applied frequency. Notably, the dielectric constant shows a significant decrease with increasing frequency for all compositions, a common behaviour in ferrites attributed to Maxwell-Wagner interfacial polarization and Koops' phenomenological theory[28,29]. At lower frequencies, the polarization mechanisms (electronic, ionic, dipolar, and space charge) contribute more effectively to the dielectric constant, resulting in higher values[30,31]. As the frequency increases, these polarization mechanisms lag behind the alternating electric field, leading to a decrease in the dielectric constant. 1 The observed variations in the initial high dielectric constant values across the samples (GK6 to GK10) are likely influenced by factors such as the concentration of charge carriers, the homogeneity of the microstructure, and the presence of defects, all of which are affected by the changing magnesium content. Similarly, the dielectric loss also decreases with increasing frequency, which is associated with the reduction in the energy required for dipole alignment at higher frequencies[32-35]. The differences in the magnitude of dielectric loss among the samples could be attributed to variations in conductivity and the density of imperfections within the ferrite lattice, which are sensitive to the compositional changes introduced by magnesium substitution. The exceptionally high dielectric constant and loss values observed for GK8, GK9, and GK10 at lower frequencies suggest the presence of enhanced polarization effects or possibly higher conductivity in these compositions compared to GK6 and GK7.

CONFLICT OF INTERESTS

None.

ACKNOWLEDGMENTS

The authors would like to express their gratitude to CIC Amravati for XRD and FTIR studies, USIC (Alagappa University) for carrying out the Room Temperature Magnetic analysis, and APRC Tirupattur for the dielectric spectroscopy. They also acknowledge the support of the college administration and the provision of necessary facilities for the research.

REFERENCES

Narang, Sukhleen Bindra, and Kunal Pubby. "Nickel spinel ferrites: a review." Journal of Magnetism and Magnetic Materials 519 (2021): 167163.

Dhiman, Pooja, et al. "Basics of ferrites: types and structures." Ferrites and Multiferroics: Fundamentals to Applications (2021): 1-25.

Aman, Salma, et al. "Synthesis and characterization of copper-based spinel ferrites for high frequency applications." Journal of Magnetism and Magnetic Materials 547 (2022): 168778.

Ramadan, Rania, Vuk Uskoković, and Mai M. El-Masry. "Triphasic CoFe2O4/ZnFe2O4/CuFe2O4 nanocomposite for water treatment applications." Journal of Alloys and Compounds 954 (2023): 170040.

Fatima, Gul, et al. "Mn-doped BaFe12O19 nanoparticles synthesis via micro-emulsion route: solar light-driven photo-catalytic degradation of CV, MG and RhB dyes and antibacterial activity." Materials Research Bulletin 168 (2023): 112491.

Gaffar, Shayista, Amit Kumar, and Ufana Riaz. "Synthesis techniques and advance applications of spinel ferrites: A short review." Journal of Electroceramics 51.4 (2023): 246-257.

Bielan, Zuzanna, et al. "Application of spinel and hexagonal ferrites in heterogeneous photocatalysis." Applied Sciences 11.21 (2021): 10160.

Katoch, Gaurav, et al. "Crystal structure, synthesis, properties and potential applications of cobalt spinel ferrite: A brief review." Materials Today: Proceedings (2023).

Katoch, Gaurav, et al. "Recent advances in processing, characterizations and biomedical applications of spinel ferrite nanoparticles." Ferrite: Nanostructures with Tunable Properties and Diverse Applications 112 (2021): 62-120.

Hao, Aize, and Xueer Ning. "Recent advances in spinel ferrite-based thin films: Synthesis, performances, applications, and beyond." Frontiers in Materials 8 (2021): 718869.

El Heda, Issa, et al. "The effect of transition metal substitution on the structural, elastic, optical, electrical and dielectric properties of M0. 5Fe2· 5O4 (M= Co and Mg) synthesized by the auto combustion method." Materials Chemistry and Physics 296 (2023): 127297.

Hasan, M. S., et al. "Structural, optical, electrical and magnetic tuning based on Zn substitution at a site in yttrium doped spinel ferrites." Materials Chemistry and Physics 301 (2023): 127538.

[17]Yang, Hu, et al. "Effect of Cd2+ substitution on structural–magnetic and dielectric properties of Ni–Cu–Zn spinel ferrite nanomaterials by Sol–Gel." Molecules 28.16 (2023): 6110.

Channagoudra, Ganesha, Ajay Kumar Saw, and Vijaylakshmi Dayal. "Role of structure and cation distribution on magnetic and electrical properties in inverse spinel copper ferrite." Journal of Physics and Chemistry of Solids 154 (2021): 110086.

Almessiere, Munirah A., et al. "Impact of the indium content on structural, magnetic, and electrodynamic properties of nanocomposites based on In-substituted Sr hexaferrite and Ni–Zn spinel ferrite with excellent absorption characteristics." Ceramics International 49.8 (2023): 12885-12894.

Ikram, Salma, et al. "Role of nature of rare earth ion dopants on structural, spectral, and magnetic properties in spinel ferrites." Journal of Superconductivity and Novel Magnetism 34 (2021): 1745-1751.

Xu, C., et al. "Control of dislocation density maximizing precipitation strengthening effect." Journal of Materials Science & Technology 127 (2022): 133-143.

Fan, Haidong, et al. "Strain rate dependency of dislocation plasticity." Nature communications 12.1 (2021): 1845.

Suryawanshi, Shrikant M., et al. "A comprehensive study on structural, magnetic and dielectric properties of Ni0. 3Cu0. 3Zn0. 4Fe1. 8Cr0. 2O4 nanoparticles synthesized by sol-gel auto combustion route." Journal of Molecular Structure 1272 (2023): 134173.

Abouhaswa, A. S., et al. "Investigation of crystal structure, electrical and magnetic properties of spinel Mn-Cd ferrite nanoparticles." Journal of Inorganic and Organometallic Polymers and Materials (2022): 1-13.

Sundararajan, M., et al. "A comparative study on NiFe2O4 and ZnFe2O4 spinel nanoparticles: Structural, surface chemistry, optical, morphology and magnetic studies." Physica B: Condensed Matter 644 (2022): 414232.

Venkatesh, Nakaraboina, et al. "FTIR, optical, electrical and magnetic properties of SM3+ doped MG nano ferrites." Biointerface Res. Appl. Chem 11.6 (2021): 15037-15050.

Jadhav, Swapnil A., et al. "Visible light photocatalytic activity of magnetically diluted Ni–Zn spinel ferrite for active degradation of rhodamine B." Ceramics International 47.10 (2021): 13980-13993.

Li, Junjiao, et al. "Effect of rare earth Nd3+ doping contents on physical, structural, and magnetic properties of Co–Ni spinel ferrite nanoparticles." Journal of Rare Earths 41.11 (2023): 1746-1753.

Sharma, Anjori, et al. "Enhancing high frequency magneto-dielectric performance with exchange-coupled garnet/spinel ferrite (Y3Fe5O12/Mg0. 4Cd0. 4Co0. 2Fe2O4) composites." Nano-Structures & Nano-Objects 36 (2023): 101035.

Pham, Tuyet Nhung, et al. "Toward a comprehensive understanding of effect of cation distribution and M2+ constituent in spinel ferrite nanocrystals MFe2O4 (M= Co, Mn, and Ni) on the electrochemical response in sensitive detection of chloramphenicol." Journal of Alloys and Compounds 949 (2023): 169880.

Channagoudra, Ganesha, et al. "Study of cation distribution in La3+ and Eu3+ substituted cobalt ferrite and its effect on magnetic properties." Journal of Magnetism and Magnetic Materials 559 (2022): 169550.

Kumari, Kavita, et al. "Dielectric properties of spinel ferrite nanostructures." Ferrite Nanostructured Magnetic Materials. Woodhead Publishing, 2023. 599-631.

Paswan, Sanjeet Kumar, et al. "Electrical transport properties of nanocrystalline and bulk nickel ferrite using complex impedance spectroscopy: a comparative study." Physica Scripta 97.9 (2022): 095812.

Wang, Lu, et al. "Progress on polymer composites with low dielectric constant and low dielectric loss for high-frequency signal transmission." Frontiers in Materials 8 (2021): 774843.

Qin, Ming, Limin Zhang, and Hongjing Wu. "Dielectric loss mechanism in electromagnetic wave absorbing materials." Advanced Science 9.10 (2022): 2105553.

Wang, Lu, et al. "Progress on polymer composites with low dielectric constant and low dielectric loss for high-frequency signal transmission." Frontiers in Materials 8 (2021): 774843.

Yang, Minzheng, et al. "High-energy-density and high efficiency polymer dielectrics for high temperature electrostatic energy storage: a review." Small 18.50 (2022): 2205247.

Ashery, Adel, A. E. H. Gaballah, and Emad M. Ahmed. "Tuned high dielectric constant, low dielectric loss tangent with positive and negative values for PPy/MWCNTs/TiO2/Al2O3/n-Si." Journal of experimental nanoscience 16.1 (2021): 309-343.

Yin, Qian, et al. "Reducing intermolecular friction work: preparation of polyimide films with ultralow dielectric loss from MHz to THz frequency." Industrial & Engineering Chemistry Research 61.49 (2022): 17894-17903.